Journal of Energy Chemistry 85 (2023) 490–500

Contents lists available at ScienceDirect

Journal of Energy Chemistry

journal homepage: www.elsevier.com/locate/jechem

http://www.journals.elsevier.com/journal-of-energy-chemistry/

The role of copper in enhancing the performance of heteronuclear diatomic catalysts for the electrochemical CO_2 conversion to C_1 chemicals

Qi Zhao [a], Rachel Crespo-Otero [b,*], Devis Di Tommaso [a,*]

[a] Department of Chemistry, School of Physical and Chemical Sciences, Queen Mary University of London, London E1 4NS, UK
[b] Department of Chemistry, University College London, London WC1H 0AJ, UK

ARTICLE INFO

Article history:
Received 3 May 2023
Revised 18 June 2023
Accepted 26 June 2023
Available online 6 July 2023

Keywords:
Electrocatalytic CO_2 reduction
Single atom catalysts
Diatomic catalysts
Graphene
Density functional theory calculations

ABSTRACT

Diatomic catalysts (DACs) with two adjacent metal atoms supported on graphene can offer diverse functionalities, overcoming the inherent limitations of single atom catalysts (SACs). In this study, density functional theory calculations were conducted to investigate the reactivity of the carbon dioxide (CO_2) reduction reaction (CO_2RR) on metal sites of both DACs and SACs, as well as their synergistic effects on activity and selectivity. Calculation of the Gibbs free energies of CO_2RR and associated values of the limiting potentials to generate C_1 products showed that Cu acts as a promoter rather than an active catalytic centre in the catalytic CO_2 conversion on heteronuclear DACs (CuN_4-MN_4), improving the catalytic activity on the other metal compared to the related SAC MN_4. Cu enhances the initial reduction of CO_2 by promoting orbital hybridization between the key intermediate *COOH 2*p*-orbitals and the metals 3*d*-orbitals around the Fermi level. This degree of hybridization in the DACs CuN_4-MN_4 decreases from Fe to Co, Ni, and Zn. Our work demonstrates how Cu regulates the CO_2RR performance of heteronuclear DACs, offering an effective approach to designing practical, stable, and high-performing diatomic catalysts for CO_2 electroreduction.

1. Introduction

The development of efficient routes for the conversion of carbon dioxide (CO_2) is an attractive research topic, as it offers the potential to mitigate climate change [1,2], generate high-value products from a cheap, clean, and abundant resource [3,4], and facilitate the realization of an artificially closed carbon loop [5]. The electrochemical CO_2 reduction reaction (CO_2RR) has arisen as an attractive strategy for the CO_2 conversion [6–8]. If coupled with electricity from renewable sources (wind, solar, or hydro power plants), the CO_2RR could achieve a carbon-neutral energy cycle in mild condition generating C_1 products such as formic acid (HCOOH), carbon monoxide (CO), methane (CH_4), methanol (CH_3OH), and C_{2+} substances such as ethylene (C_2H_4), ethanol (C_2H_5OH), and others [2,3]. While significant progress has been made in the development of electrocatalytic CO_2RR, there are still several scientific challenges that need to be addressed, including the activation of the CO_2 molecule, the sluggish kinetics due to multiple concerted proton-electron transfer (CPET) steps, the low Faradaic efficiency (FE), and the competition from the hydrogen evolution reaction (HER, $H^+ + 2e^- \rightarrow H_2$) [9–13]. These challenges can be addressed by developing advanced catalytic systems with high energy efficiency and conversion rates [14].

Atomically dispersed 3*d* earth-abundant metals (Fe, Co, Ni, Cu, and Zn) on carbon supports, such as graphene, are single atom catalysts (SACs) that exhibit better selectivity towards CO_2RR over the HER than surface catalysts [15–22]. The high conductivity and specific atom environment of carbon supports contribute to their effectiveness in dispersing metal atoms and promoting CO_2RR [23–26]. Metal-nitrogen-doped carbon materials (MNCMs) are particularly promising, as they have unique electronic and geometric structures that allow for the anchoring of dispersed atoms [27,28]. MNCMs have a high density of effective active sites and a low coordination environment for the central metal, which enhances their electrocatalytic activity and selectivity [27,29].

Diatomic catalysts (DACs) are a natural extension of SACs and have gained considerable attention as an enhanced catalytic platform due to the synergistic effects of metals at adjacent active sites [30–34]. SACs are limited in their ability to break linear scaling relationships between various adsorption and desorption intermediates (*COOH and *CO) during CO_2RR. Recent research also discusses the fundamental limitations in the electrochemical

* Corresponding authors.
E-mail addresses: r.crespo-otero@ucl.ac.uk (R. Crespo-Otero), d.ditommaso@qmul.ac.uk (D. Di Tommaso).

https://doi.org/10.1016/j.jechem.2023.06.029

CO_2-to-CO conversion on SACs [35]. DACs can overcome this limitation by providing greater control over the catalytic properties [36,37]. Graphene (Gra) based DACs, similar to previously reported SACs, have also been realized and characterized experimentally. These experimental studies provide useful models for theoreticians to investigate [32,38–44].

Currently, copper (Cu) is the only reported CO_2RR catalyst that can effectively promote multiple carbon products [45,46]. However, the formation of a mixture of primary products and competition with the HER present significant challenges for Cu electrocatalysts. In addition, monometallic Cu-based catalysts often require high overpotentials for CO_2RR, which further limits their potential applications [47–49]. On the other hand, SACs with metal centres other than Cu (such as Fe, Co, Ni, and Zn) typically produce HCOOH or CO as the main products. In some cases, these SACs have been found to produce highly reduced chemicals such as CH_3OH [25,50,51]. Furthermore, experimental electrochemical studies of heteronuclear $FeCuN_6$/Gra [52], $NiCuN_6$/Gra [53], ZnCuN6/Gra [38], and $CoCuN_6$/Gra [43] reported that DACs improved the catalytic CO_2RR activity compared to MN_4/Gra SACs.

Table S1 summarizes more than thirty studies of DACs for the CO_2RR. Despite the significant interest in the synergistic effect of these adjacent metal sites on achieving high CO_2RR performance, there is a lack of the atomic-level detail into their separate roles of the metals. Recently, Yi et al. demonstrated that CuN_4-CoN_4 DACs achieve high-efficiency CO_2 electroreduction to CO at industrial-level current density [43]. Moreover, a recent computational study conducted by Wei et al. showed the synergistic effect of Cu/Fe can improve Fe atom catalytic activity [54]. This research motivated us to further investigate the synergistic effect of copper with 3*d* non-precious metals (such as iron, cobalt, nickel, zinc), in order to rationalize the role of the two metal centres in DACs during the CO_2RR.

In this paper, we investigated the mechanism of CO_2RR catalysed on CuN_4-MN_4 DACs and MN_4 SACs with different metals (M = Cu, Fe, Co, Ni, and Zn) using density functional theory (DFT) calculations. Our goal was to elucidate the role of the separate metal sites in the CO_2RR. The results indicate that Cu is an excellent promoter for CO_2RR, significantly improving the Fe, Co, Ni, and Zn catalytic performance in DACs on producing C_1 products compared to the corresponding SAC counterpart. The promotion effect gradually weakens from Fe to Co to Ni to Cu to Zn, as demonstrated by the hybridization between the 2*p* orbitals of intermediates and the 3*d* orbitals of metals. In this work, we aim to illustrate a new mechanism for Cu on CO_2RR, which differs from the traditional concept of Cu as the CO_2RR active centre.

2. Computational details

2.1. Density functional theory calculations

We performed DFT calculations using the Vienna ab initio simulation package (VASP) [55,56]. The cut-off energy of the plane-waves was 500 eV. The exchange-correlation interactions were described by the optPBE-vdW functional [57,58]. A 3 × 3 × 3 *k*-point mesh was used for geometry optimizations and a 15 × 15 × 1 *k*-point mesh was used for the static calculation and for the analysis of the electron and orbital [59]. Structural relaxations were performed until the maximum residual force on each atom was less than 0.05 eV $Å^{-1}$. Bader charge analysis was carried out with the core charges included [60]. The metal *d* band centre ($\varepsilon(d)$), projected density of states (PDOS), and Bader analysis were calculated using VASPKIT [61].

The changes of the Gibbs free energy (ΔG) of each step were computed to determine the most favourable reaction pathway. For processes involving proton-electron transfer, the reaction energy was calculated using the computational hydrogen electrode (CHE) method proposed by Nørskov and co-workers [62]. The free energy differences of the processes were computed according to the following expression.

$$\Delta G = \Delta E_{\mathrm{DFT}} + \Delta E_{\mathrm{ZPE}} - T\Delta S \tag{1}$$

where ΔE_{DFT} is the total energy difference from the DFT calculations, ΔE_{ZPE} is the zero-point energy (ZPE) correction from the frequency analysis, and $T\Delta S$ is the entropy contribution at the temperature (T) of 300 K.

The limiting potential U_{L} is an important factor for evaluating the catalytic activity and is calculated by

$$U_L = -\frac{\Delta G_{\max}}{ne} \tag{2}$$

where $\Delta G_{\max}$ is the relative change of the Gibbs free energy of the rate-determining step, n is the number of electrons transferred, and e is the electron charge.

The thermodynamic stability of the SACs and DACs was estimated by computing the binding energy, cohesive energy, and formation energy. These energy descriptors were previously used to evaluate the stability of two-dimensional (2D) transition metal porphyrin sheets [63]. The binding energies (E_{b}) for the SACs and DACs were determined using the following equations.

$$E_{\mathrm{b}} = E_{\mathrm{M-Gra}} - E_{\mathrm{M}} - E_{\mathrm{Gra}} \tag{3}$$

$$E_{\mathrm{b}} = E_{\mathrm{Cu/M-Gra}} - E_{\mathrm{M}} - E_{\mathrm{Cu}} - E_{\mathrm{Gra}} \tag{4}$$

where the $E_{\mathrm{M\text{-}Gra}}$, $E_{\mathrm{Cu/M-Gra}}$, E_{M}, E_{Cu}, and E_{Gra} are the energies of the SAC, DAC, metal, Cu, and graphene framework without the metal atom(s), respectively. The cohesive energy (E_{c}) was computed according to the following equation.

$$E_{\mathrm{c}} = \frac{E_{\mathrm{M(bulk)}}}{N} - E_{\mathrm{M}} \tag{5}$$

where the $E_{\mathrm{M(bulk)}}$ is the energy of the bulk unit cell containing N atoms and E_{M} is the energy of the isolated metal atom in vacuum. The formation energy (E_{f}) was computed according to

$$E_{\mathrm{f}} = E_{\mathrm{M/Gra}} - N_{\mathrm{M}}\mu_{\mathrm{M}} - N_{\mathrm{C}}\mu_{\mathrm{C}} - N_{\mathrm{N}}\mu_{\mathrm{N}} \tag{6}$$

where the $E_{\mathrm{M/Gra}}$ is the energy of M/Gra, N_{M}, N_{C}, and N_{N} are the number of M, C, and N atoms in the unit cell, respectively, and μ_{M}, μ_{C}, and μ_{N} are the chemical potentials of the M, C, and N atoms, which were obtained from the energy calculation of transition metal single atom, graphene ($\mu_{\mathrm{C}} = E(\mathrm{Gra})/N_{\mathrm{C}}$), and N_2 ($\mu_{\mathrm{N}} = E(N_2)/2$), respectively.

The electrochemical stability of SACs and DACs was evaluated by computing the dissolution potential (U_{diss}) of the metal [64]. For SACs, this property was calculated with the following formula.

$$U_{\mathrm{diss}}(\mathrm{M}) = U^{\circ}_{\mathrm{diss}}(\mathrm{M,bulk}) - \frac{\left(E_{\mathrm{M/Gra}} - \frac{E_{\mathrm{M(bulk)}}}{N} - E_{\mathrm{Gra}}\right)}{ne} \tag{7}$$

where $U^{\circ}_{\mathrm{diss}}(\mathrm{M,bulk})$ is the standard dissolution potential of the metal of the bulk metal and n is the number of electrons involved in the dissolution process. In this work, the values of $U^{\circ}_{\mathrm{diss}}(\mathrm{M,bulk})$ were taken from Guo et al. [65] and n was set to 2. For the CuN_4-MN_4 DACs, the dissolution potential of one of the two metals, for example M, was computed according to the following formula [54].

$$U_{\mathrm{diss}}(\mathrm{M}) = U^{\circ}_{\mathrm{diss}}(\mathrm{M,bulk}) - \frac{\left(E_{\mathrm{Cu/M-Gra}} - E_{\mathrm{Cu/\square-Gra}} - \frac{E_{\mathrm{M(bulk)}}}{N}\right)}{ne} \tag{8}$$

where $E_{Cu/\square-Gra}$ is the energy of the framework without the metal atom.

2.2. Atomistic models

Wang et al. reported the formation of stable bimetallic FeFe-N_6 structures under low hydrogen concentration [32]. These structures have high metal formation energy and can inhibit the formation of clusters. In this study, we built the MCu-N_6 (M = Fe, Co, Ni, Cu, and Zn) models of DACs shown in Fig. 1, exhibiting the favourable structures reported by Wang et al. [32]. In addition, we built nitrogen-coordinated SACs including FeN_4, CoN_4, NiN_4, CuN_4, and ZnN_4 to investigate the individual performance of each metal and the role of Cu in DACs in CO_2 activation and reduction. Moreover, our calculated structures well match to experiment catalyst characteristics, such as NiCuN6/Gr [53], ZnCuN6/Gra [38], and CoCuN6/Gra [43]. Details of the 4 × 4 and 5 × 5 supercells used to model the SACs and DACs, respectively, are shown in Fig. S1.

3. Results and discussion

3.1. Stability and geometry features of SACs and DACs models

During the high-temperature heat treatment of MNCMs, transition metals tend to aggregate, which promotes the HER over the CO_2RR [66–68]. Thus, forming stable dispersed atomic catalysts is essential for CO_2RR. Consequently, we explored the energetics of doping metals into MNCMs using non-metal coordination to regulate metal stability in MN_4. This involved substituting N with C (M/Gra), substituting N with O (MN_2O_2/Gra), and nitrogen coordinated MN_4 structure (MN_4/Gra). All these substitution patterns were obtained experimentally [69].

As reported in Fig. 2 and Table S2, the formation energies of metal coordinated with four carbon atoms (MC_4) are −4.95 eV (Fe), −4.47 eV (Co), −4.40 eV (Ni), −3.79 eV (Cu), and −2.70 eV (Zn). When considering oxygen substitution (M−N_2O_2), the formation energies are −3.37 eV (Fe), −3.47 eV (Co), −3.09 eV (Ni), −1.62 eV (Cu), and −0.73 eV (Zn), which are higher than the values obtained for MC_4. However, the most stable MNCMs with the most negative formation energies are found for Fe (−5.90 eV), Co (−5.75 eV), Ni (−6.24 eV), Cu (−3.80 eV), and Zn (−3.21 eV), when coordinated with nitrogen atoms (MN_4).

The coordination environment of the metal centre in MN_4 and MN_2O_2 features a D_{4h} symmetry in the square-planar field.

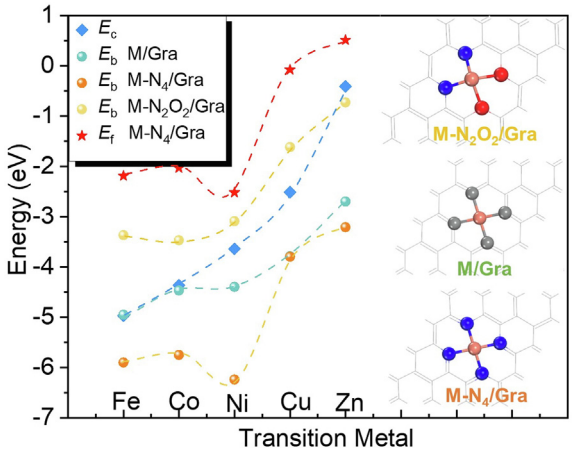

Fig. 2. Thermodynamic stability of the SACs M−C_4, M−N_2O_2, and M−N_4. Values of the cohesive energy (E_c) of the transition metal (M) bulk, binding energy between M and graphene (Gra) (E_b), and formation energy (E_f) of M−Gra. Red, blue, grey, and orange spheres are O, N, C, and M atoms (M = Fe, Co, Ni, Cu, and Zn).

Insights into the *d*-orbital splitting were obtained by computing the PDOS of the *d* orbitals of the metal centre (Fig. S2), in order to determine the energy difference between the *d* orbitals with maximum PDOS (Table S3). Except for Zn, where all the *d* levels are filled, the *d*-orbital splitting seems to be more significant in MN_4 than in MN_2O_2, indicating stronger interaction between M and N_4 than M and N_2O_2, thus forming a more stable geometric structure, in agreement with the stability analysis of the SACs in Fig. 2.

To investigate the catalytic activity of individual metals and the synergistic effect of these metals on the CO_2RR, we constructed SACs with MN_4 structures and DACs with CuN_4-MN_4 structures. According to the values of the dissolution potential of the SACs (Table S2) and DACs (Table S4), all of the catalysts have more positive values of U_{diss} than the experimentally applied potential for CO_2RR (from −0.2 to 1.2 V) [54], suggesting that these active sites are all stable against dissolution in the CO_2RR. Only ZnN_4 has a negative U_{diss} (−1.02 V), whereas all other SACs and DACs have U_{diss} above zero.

Other geometric features of the DACs models, including the distance between the two metal atoms in the DACs (Table S5), the electronic properties of SACs and DACs, such as the values of the *d*-band centre of the metal atoms (Table S6), and the Bader charges

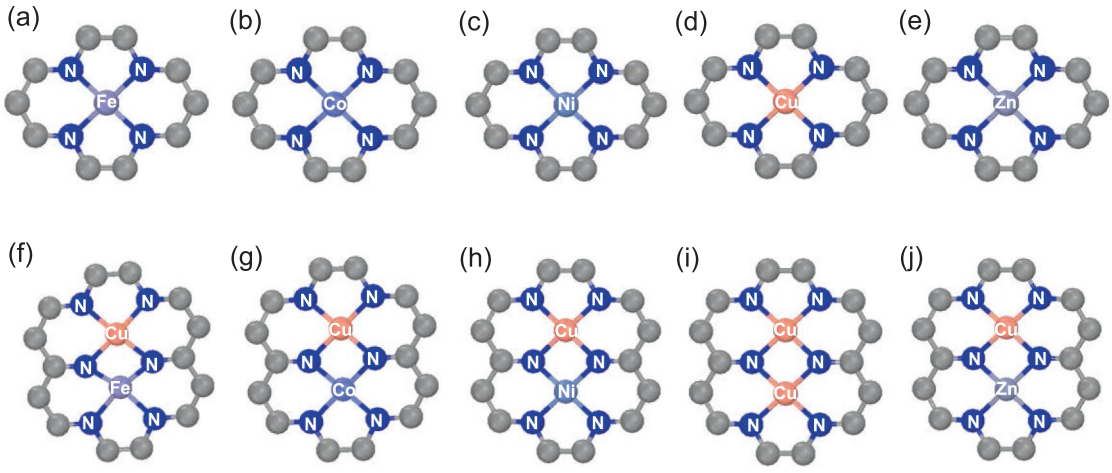

Fig. 1. Optimized structures of the metal-doped carbon SACs (a) Fe-N_4, (b) Co-N_4, (c) Ni-N_4, (d) Cu-N_4, (e) Zn-N_4, and DACs (f) FeCu-N_6, (g) CoCu-N_6, (h) NiCu-N_6, (i) CuCu-N_6, and (j) ZnCu-N_6.

(Table S7), are also reported in Supporting Information. Another important point is to distinguish whether the two metal atoms in CuN_4-MN_4 function as a bimetallic central or a diatomic catalyst. The distance between diatoms varies, ranging from 2.25 Å for Cu-Fe to 2.59 Å for Cu-Zn (Table S5). In the Fourier transform extended X-ray absorption fine structure (FT-EXAFS) spectra, the Fe-Cu peak appears at 2.0 Å [70]. However, in our CuN_4-FeN_4 model, the Cu-Fe distance measures 2.25 Å indicating a diatomic structure. Similarly, other diatomic catalysts, such as Cu-Co (d_{Cu-Co} = 2.52 Å in this DFT study vs. d_{Cu-Co} = 2.4–2.5 Å from experiment [43]), Cu-Ni (d_{Cu-Ni} = 2.55 Å in this DFT study vs. d_{Cu-Ni} = 2.40 Å from experiment [53]), and Cu-Zn (d_{Cu-Zn} = 2.59 Å in this DFT study vs. d_{Cu-Zn} = 2.40 Å from experiment [38]) possess a diatom structure instead of a bimetallic structure.

3.2. Catalytic performance of the Cu-N_4 SAC and homonuclear CuN_4-CuN_4 DAC

The Gibbs free energy diagrams of the CO_2-to-CO conversion and its competitive HER on the SACs with M−N_4, M−N_2O_2, and M−C_4 coordination are shown in Figs. S3–S6. The results show that the M−N_4 structures, the most stable structure of the SACs, are also more selective for the CO_2RR. Therefore, in this section, we compare the performance of the N-coordinated Cu-N_4 SAC and homonuclear CuN_4-CuN_4 DAC for the conversion of CO_2 to C_1 molecules, including CO, HCOOH, CH_3OH, and CH_4 (Fig. 3). As shown in Fig. 3(a), the first step in the CO_2RR to CO on SAC CuN_4 is the adsorption of CO_2 (CO_2 → $*CO_2$), which requires 0.37 eV of energy. The next step, a CPET process to form COOH ($*CO_2 + H^+ + e^-$ → *COOH), requires 1.09 eV and is rate-limiting in the CO_2-to-CO conversion path. Subsequently, the CPET step to form H_2O and CO ($*COOH + H^+ + e^-$ → $*CO + H_2O$) is an exothermic process (−0.20 eV). The *CO desorption from the single Cu site is also favourable (−0.24 eV). Turning the discussion to the CuN_4-CuN_4, with adsorption energy of 0.14 eV, the CO_2 adsorption on the DAC is more favourable than on the CuN_4 SAC. However, the slightly stronger binding of $*CO_2$ does not improve the subsequent reduction process to form *COOH, as the free energy required to form *COOH (1.69 eV) is higher than that on a single Cu site (1.09 eV).

The competition between CO desorption and further reduction of CO to form CH_3OH and CH_4 influences the selectivity of C_1 products. Even if *CO binds stronger on the CuN_4-CuN_4 DAC (E_{des} = 0.09-eV) than on the SAC CuN_4 (E_{des} = −0.24 eV), the diatomic catalysts show less significant improvement in the subsequent CPET steps to form $*CH_3OH$ (green line in Fig. 3c) and $*CH_4$ (brown line in Fig. 3d) from the *CO intermediate compared to the same conversion paths on the SAC CuN_4. The only lower C_1 pathway catalysed by the CuN_4-CuN_4 DAC is towards *HCOOH, where the O-coordinated (*OCHO) intermediate is significantly stabilized (Fig. S7), leading to the formation of formic acid. This finding is consistent with the DFT results of Wang et al., which reported that a Cu dimer anchored in a graphite-CN monolayer (Cu_2@CN) has superior catalytic activity for the CO_2 conversion to HCOOH and ethylene (C_2H_4) than the corresponding single-atom counterpart (Cu@CN) [71]. However, the consideration of C_2 products is beyond the scope of this work because of the difficulties in coupling reactions on single dispersed sites on SACs (Table S1).

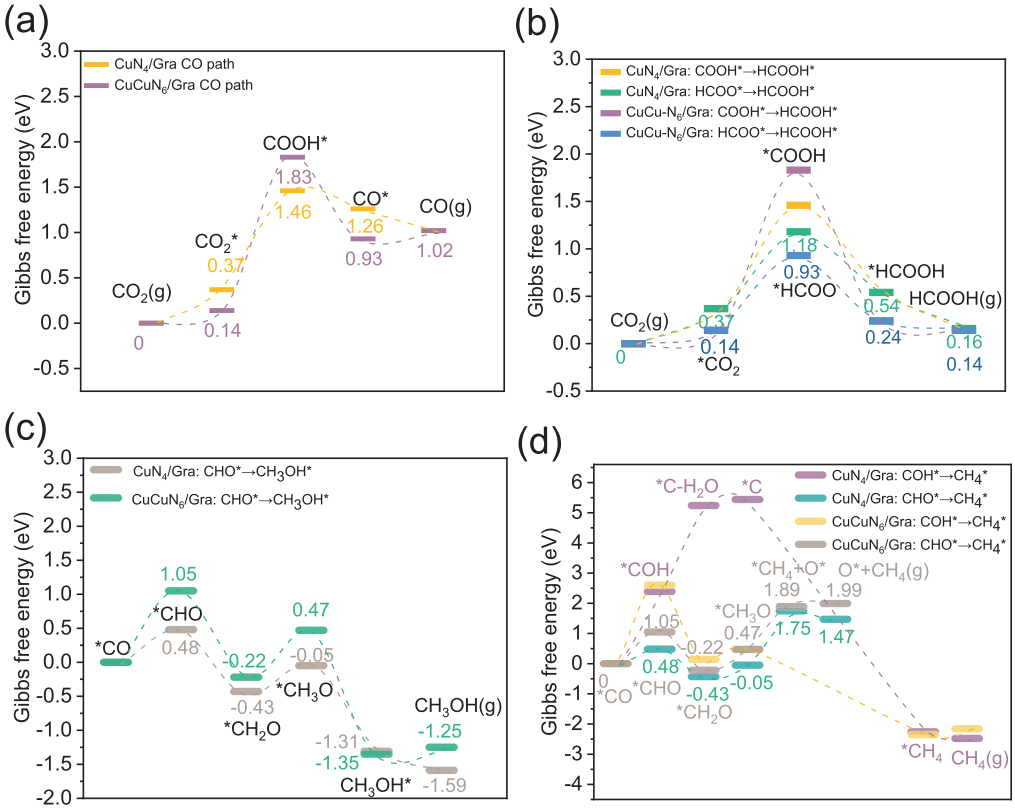

Fig. 3. Free energy diagram of CO_2RR on Cu-Cu DACs leading the formation of the following C_1 products. (a) Carbon monoxide [$CO_2(g)$ → $*CO_2 + H^+ + e^-$ → $*COOH + H^+ + e^-$ → $*CO + H_2O$ → CO(g)]; (b) formic acid [$CO_2(g)$ → $*CO_2 + H^+ + e^-$ → $*HCOO + H^+ + e^-$ → *HCOOH → HCOOH(g)]; (c) methanol [$*CO + H^+ + e^-$ → $*CHO + H^+ + e^-$ → $*CH_2O + H^+ + e^-$ → $*CH_3O + H^+ + e^-$ → $*CH_3OH$ → $CH_3OH(g)$]; (d) methane [$*CO + H^+ + e^-$ → $*CHO + H^+ + e^-$ → $*CH_2O + H^+ + e^-$ → $*CH_3O + H^+ + e^-$ → $*CH_4 + O^*$ → $CH_4(g)$].

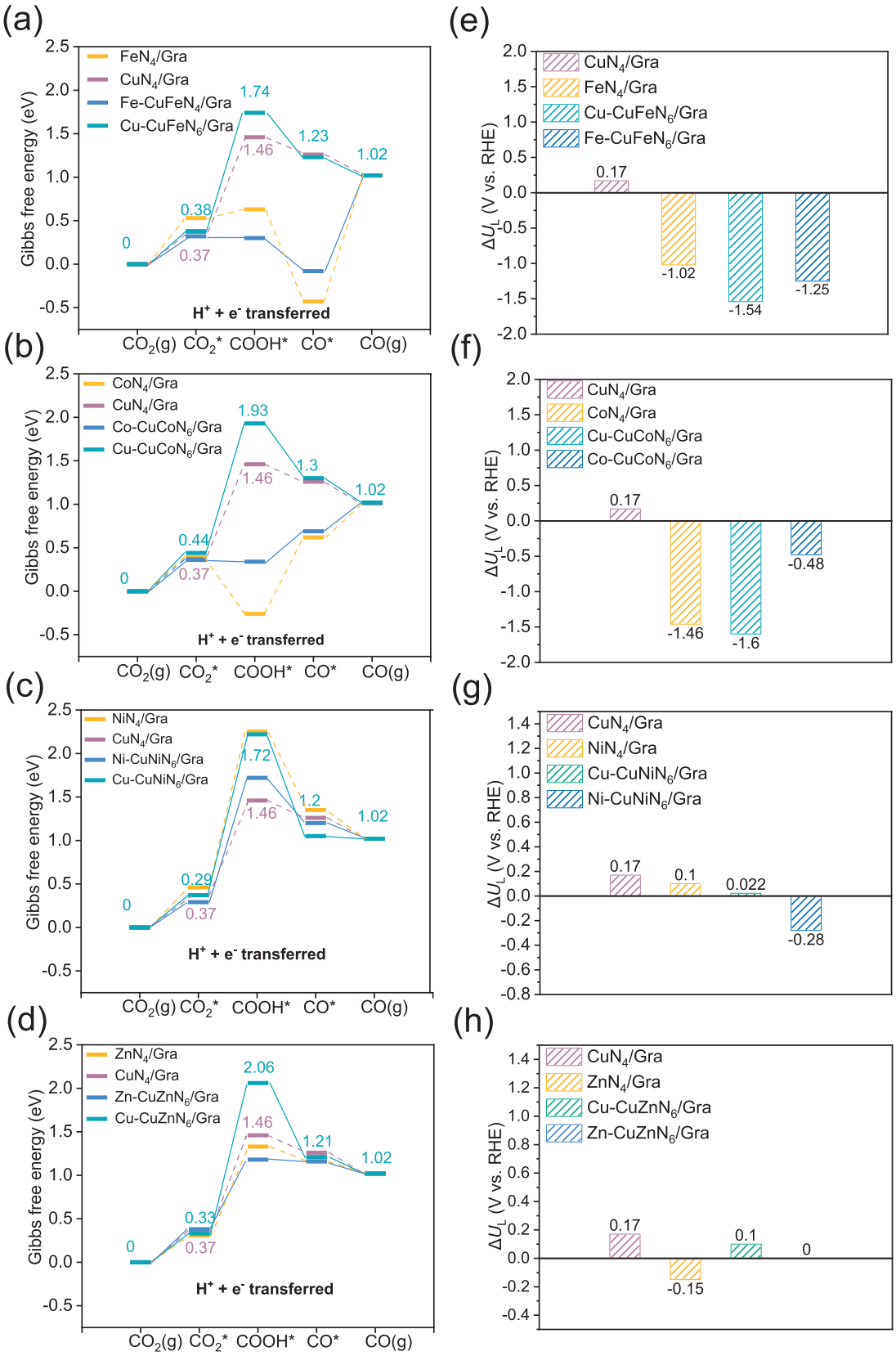

Fig. 4. (a–d) Free energy diagrams of the CO_2RR to CO on the SACs MN_4 and DACs MN_4-CuN_4. (e–h) $\Delta U_L = U_L(CO_2RR) - U_L(HER)$ for the CO_2RR into CO on SACs and DACs; a positive value of ΔU_L corresponds to selectivity towards the CO_2RR. Cu-$CuMN_6$/Gra and M−$CuMN_6$/Gra indicate that the catalytic centres of the DACs for the CO_2RR are Cu and M (M = Fe, Co, Zn, and Ni), respectively.

3.3. Catalytic performance of the M–N_4 SACs and heteronuclear CuN_4-MN_4 DACs

The Gibbs free energy (ΔG) diagrams of the CO_2RR to CO on the SACs M–N_4 and heteronuclear CuN_4-MN_4 DACs (M = Fe, Co, Ni, and Zn) are compared in Fig. 4. The ΔG values of the elementary steps of the CO_2RR on the SACs and DACs to form CO, HCOOH, CH_3OH, and CH_4 are summarized in Table S8 for the SAC and Table S9 for the DAC; the G values for gas molecule and initial reduction intermediates are listed in Tables S10–S15. The reactions taking place on both Cu and M sites were considered for the DACs.

On the Cu site of the CuN_4-MN_4 DACs, the CPET step ($*CO_2 + H^+ + e^- \rightarrow *COOH$) is rate-determining (maximum value of ΔG), with positive reaction free energies of 1.36 eV for CuN_4-FeN_4, 1.49 eV for CuN_4-CoN_4, 1.85 eV for CuN_4-NiN_4, and 1.73 eV for CuN_4-ZnN_4 (Fig. 4a–d). All these ΔG values are higher than that on the SAC CuN_4 (1.09 eV). The Cu site in DACs CuN_4-MN_4 is significantly less active for the initial reduction of CO_2 to CO, while the opposite is observed for the other metal sites (Fe, Co, Ni, and Zn) compared to their respective SACs (MN_4, M = Fe, Co, Ni, and Zn). Fig. 4 shows that the energy required for the reaction $*CO_2 + H^+ + e^- \rightarrow *COOH$ is −0.02 eV on both Fe and Co sites of CuN_4-FeN_4 and CuN_4-CoN_4. The Ni site of CuN_4-NiN_4 requires a higher energy of 1.43 eV, and the Zn site of CuN_4-ZnN_4 requires 0.80 eV. All cases are more favourable than the corresponding SACs MN_4, including FeN_4 (0.10 eV), CoN_4 (−0.65 eV), NiN_4 (1.79 eV), and ZnN_4 (1.02 eV). Notice that even though the reaction energy on CoN_4 is more negative (−0.65 eV) than on CoN_4-CuN_4 (−0.02 eV), the *COOH intermediate could bind too strongly to the catalyst sites and impede its further conversion. The above results indicate that in the CuN_4-MN_4 DACs, M (Fe, Co, Ni, and Zn) is the active site for the CO_2RR, and the proximity of the Cu to M leads to an improved CO_2RR performance than M in SACs MN_4.

To quantify the selectivity of SACs and DACs towards the formation of carbon products rather than H_2, we have used the difference between the limiting potentials U_L calculated using Eq. (2) of the CO_2RR and HER, $\Delta U_L = U_L(CO_2RR) - U_L(HER)$ [72–74], as shown in Fig. 4(e–h). The limiting potential refers to the minimum reverse electrode potential required to overcome the CPET step associated with the largest positive free energy change, namely, the formation of *COOH (Fig. 4a–d). Consequently, a positive ΔU_L would indicate that the largest Gibbs free energy step during the CO_2RR is smaller than the largest one during the HER, leading to a greater selectivity for carbon products over H_2 formation. Fig. 4(e–h) shows that the ΔU_L value of the Cu active site in the CuN_4-MN_4 DAC (−1.54 V) is much more negative than that in the CuN_4 SAC (0.17 V). This difference is particularly pronounced for Cu compared to the other metals in CuN_4-MN_4 and MN_4. Therefore, the Cu site in DACs favour the hydrogen evolution process rather than CO_2 conversion. The finding challenges the concept of Cu as the active centre for CO_2RR and suggests that Cu could instead play a role in promoting the catalytic CO_2RR on the adjacent M site.

3.4. Reaction pathways of the CO_2RR to C_1 products on SACs and DACs

In addition to the two-electron reduction mechanisms generating CO and HCOOH, we have computed the six- and eight-electron reduction pathways leading to the formation of CH_3OH and CH_4 (Fig. 5). In this study, we only focused on C_1 products (Table S1) not only because C_2 products are rarely observed on atomically dispersed electrocatalysts due to the lack of suitable adsorption sites for C–C coupling of C_2 intermediates [75], but also out of the practical consideration. In fact, a techno-economic evaluation of low-temperature CO_2 electrolysis showed that achieving high yields of C_1 products is competitive to conventional processes compared to C_2 products, which production has substantially higher costs [76].

Upon CO_2 adsorption, the first CPET step leads to the *OCHO or *COOH intermediates. The second CPET step forms HCOOH ($*OCHO + H^+ + e^- \rightarrow *HCOOH$) or CO ($*COOH + H^+ + e^- \rightarrow *CO + H_2O$). The pathway leading to CO has been discussed in Section 3.3. On DACs, the CPET step ($CO_2 + H^+ + e^- \rightarrow *OCHO$) in Fig. 6(a, d, g, and j) has reaction free energies of −0.07 eV on FeN_4-CuN_4, 0.20 eV on CoN_4-CuN_4, 1.25 eV on NiN_4-CuN_4, and −0.21 eV on ZnN_4-CuN_4. In comparison, the reaction free energies of the CPET step ($CO_2 + H^+ + e^- \rightarrow *COOH$) are −0.02 eV on FeN_4-CuN_4, −0.02 eV on CoN_4-CuN_4, 1.43 eV on NiN_4-CuN_4, and 0.80 eV on ZnN_4-CuN_4 (Table S9).

Fig. 6 also reports the CPET steps involved in the two different CO reduction reaction (CORR) pathways: $*CO + H^+ + e^- \rightarrow *CHO$; $*CO + H^+ + e^- \rightarrow *COH$. The free energies of formation of *CHO and *COH on the FeN_4 SAC are 1.27 eV (Fig. 6b) and 2.61 eV (Fig. 6c), respectively. Similarly, the reaction energy for $*CO + *H \rightarrow *COH$ on the Fe site of DAC CuN_4-FeN_4 is 2.31 eV (Fig. 6c), while the reaction energy for $*CO + *H \rightarrow *CHO$ is only 0.65 eV (Fig. 6b). These results suggest that on both SAC FeN_4 and DAC CuN_4-FeN_4, the proton is preferentially transferred to the carbon rather than the oxygen atom of CO. The reduction of *CO to *CHO is consistently more favourable than that of *CO to *COH on Co (Fig. 6e and f), Ni (Fig. 6h and i), and Zn sites (Fig. 6k and l) in both SACs and DACs.

In summary, carbon end reduction is the main pathway for the CO_2 to C_1 products on Fe, Co, Ni, Cu, and Zn atomic catalysts (MN_4 and CuN_4-MN_4). Moreover, all reaction pathways to C_1 products

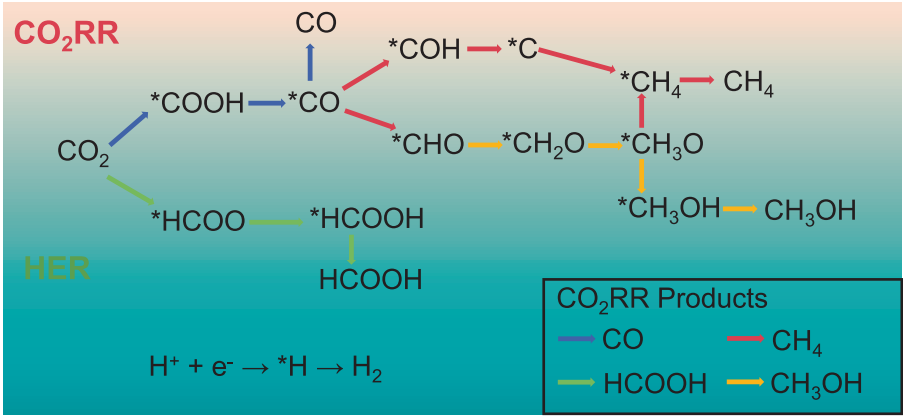

Fig. 5. The reaction pathways of the CO_2RR into the C_1 products CO, HCOOH, CH_3OH, and CH_4, and of the HER.

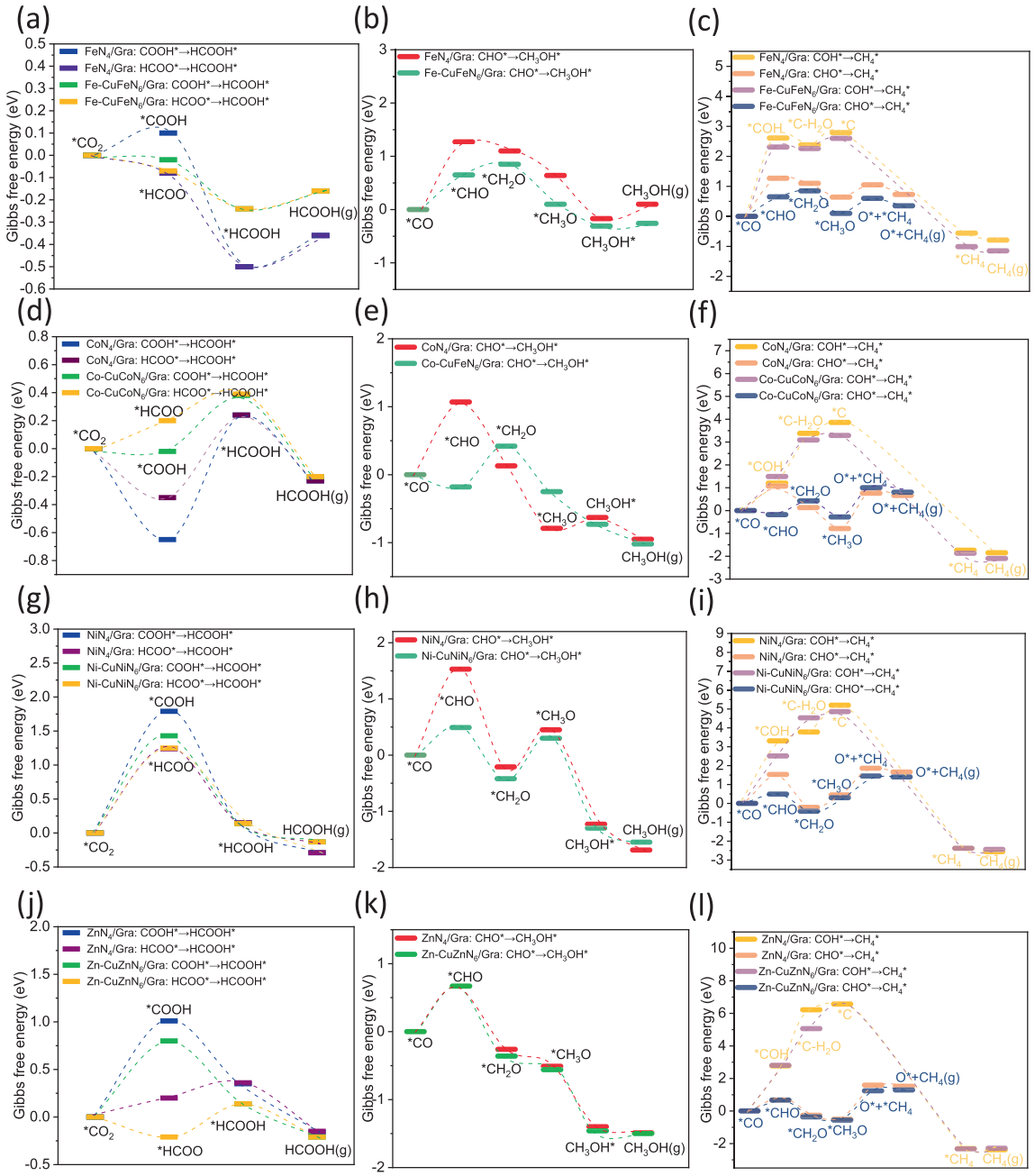

Fig. 6. Free energy diagrams of the CO_2RR to HCOOH, CH_3OH, and CH_4 on SACs and DACs: (a–c) FeN_4 and CuN_4-FeN_4; (d–f) CoN_4 and CuN_4-CoN_4; (g–i) NiN_4 and CuN_4-NiN_4; (j–l) ZnN_4 and CuN_4-ZnN_4. M−$CuMN_4$/Gra labels the metal site (M) of the DAC on which the CO_2RR reaction occurs.

have been improved on CuN_4-MN_4 compared to MN_4, indicating the promoting role of Cu. The structures of the intermediates for the CO_2RR on SACs and DACs are shown in Figs. S8 and S9, respectively.

3.5. Selectivity of CO_2RR versus HER on SACs and DACs

The difference between the limiting potentials for the CO_2RR and HER, $\Delta U_L = U_L(CO_2RR) - U_L(HER)$, is a reliable indicator of the catalyst selectivity towards these two reactions. A more positive ΔU_L indicates that the catalyst is selective for CO_2RR and more likely to produce carbon products. The computed values of ΔU_L for the CO_2RRs to C_1 molecules on SACs and DACs are summarized in Fig. 7.

The CuN_4-FeN_4 catalyst exhibits ΔU_L values of −1.25 V, −0.47 V, −0.80 V, and −0.80 V for the formation of CO, HCOOH, CH_3OH, and CH_4, respectively. These results confirm the experimentally observed high FE for HCOOH and low FE for CO on DAC CuN_4-FeN_4 by Wei et al. [52,54]. On CuN_4-CoN_4, the presence of Cu significantly improved the selectivity of the catalytic CO_2 conversion to C1 products on the Co metal site of the DACs due to the more positive ΔU_L value of CuN_4-CoN_4 than CoN_4, as shown in Fig. 7. Yi et al. have also reported that an industrial-level current density can achieve the maximum CO partial current density on a diatomic site catalysts consisting of Co-Cu hetero-diatomic pairs [43]. However, on DAC CuN_4-NiN_4, the overpotential for hydrogen evolution is lower than that on SAC NiN_4; the hydrogen evolution is preferred over CO_2 reduction on these two catalysts, despite the improve-

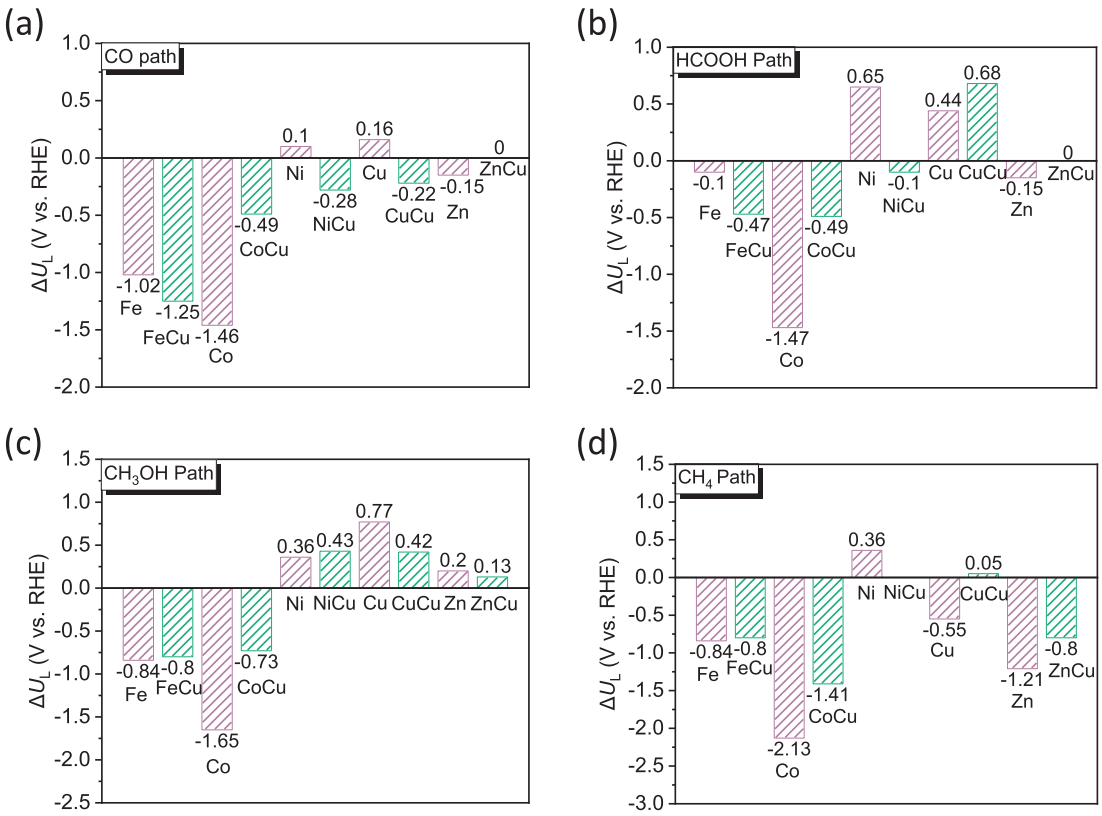

Fig. 7. Values of $\Delta U_L = U_L(CO_2RR) - U_L(HER)$ on SACs and DACs for the CO_2RRs to the C_1 products CO, HCOOH, CH_3OH, and CH_4. A positive ΔU_L indicates that the catalyst is more selective for the CO_2RR than the HER.

ment in Ni activity in the presence of Cu in the DACs shown in Fig. 6(g–i).

Among the considered DACs, CuN_4-ZnN_4 exhibits the highest selectivity towards CO, which was also proven experimentally by Hao et al. [38]. The linear relationship between the binding strength of *COOH and *CO [77] on M–N_4 and MN_4-CuN_4 in Fig. S10 shows the correlation between low CO selectivity and a large free energy of adsorption (G_{ad}) of *CO. However, the large G_{ad} of *COOH promotes the initial reduction elementary reaction ($CO_2 + H^+ + e^- \rightarrow$ *COOH). Despite the initial activation of the CO_2 molecule, the above calculations confirm that CuN_4-FeN_4 is less selective to CO, in agreement with the work reported by Wei et al. that the CuN_4-FeN_4 DAC hinders CO production [54].

3.6. The mechanism controlling the role of Cu as a promoter in the DACs

According to the *d*-band centre theory for transition metals (ε_M), a weaker filling of electrons in the antibonding orbitals strengthens the adsorption of reactants, products, and intermediates [78]. Consequently, the value of ε_M of the metals in SACs and DACs can be used to determine the synergistic effects of Cu and M on the CO_2RR performance. The computed values ε_M in SACs and DACs are reported in Fig. S11.

The *d*-band centre of Fe, Co, and Zn in heteronuclear DACs is far from the Fermi level, compared to their SACs (Fig. S11a vs. f, b vs. g, and e vs. j). Consequently, it is more favourable for products to desorb from the catalyst sites. However, for the homonuclear the Cu-Cu DAC, the *d*-band centre moves upwards to the Fermi level, compared to its SAC (Fig. S11d vs. i). This indicates that reaction species are strongly bound to the active sites, which could lead to further catalysis reactions, such as coupling to multiple carbon products. However, these reactions are outside the scope of our study. Due to the close electronegativity of Cu and Ni, the electronegativity offset [53] in CuN_4-NiN_4 leads to a better CO_2RR performance (electronegativity: Fe 1.83; Co 1.88; Ni 1.91; Cu 1.9; Zn 1.65).

As previously discussed, the initial reduction of CO_2 to form the *COOH (*$CO_2 + H^+ + e^-$) intermediate is the rate-determining step for the generation of C_1 products (Fig. 4). Therefore, the interaction between *COOH and the metal sites is critical to understanding the CO_2RR promotion mechanism on DACs. As shown in Fig. 8, there is stronger orbital hybridization (orbital overlap) between the *COOH 2*p*-orbital and the M 3*d*-orbital at the Fermi level on CuN_4-MN_4, but weaker on M–N_4. This results in the rate-limiting step of CO_2RR on CuN_4-MN_4 having a lower reaction Gibbs free energy, which is favourable for further reactions. In addition, the hybridization degree is the most significant in FeN_4-CuN_4 system and less in ZnN_4-CuN_4. Fig. 8(b, d, f, h, and j) shows that the hybridization between the *COOH 2*p*-orbital and the M 3*d*-orbital at the Fermi level under Cu regulation gradually weakens from Fe to Zn. This may be related to the interatomic electron transfer between the two metals in DACs, as shown by the charge difference between the two metals in Fig. S12. In addition to studying the shift of the *d*-band center and orbital hybridization, we also conducted Bader's atoms-in-molecules analysis of the wavefunctions generated from DFT geometry-optimized structures of all intermediates involved in the entire reaction path of the CO_2RR. For most intermediates, the Bader charges of the metals are nearly higher on DACs (red line in Fig. S12k–o) than that on SACs (black line in Fig. S12k–o). This suggests that during the CO_2RR, the interaction between the metal site M in CuN_4-MN_4 and the intermediates is more significant than in SACs. It further infers that the adjacence of Cu stimulates the catalytic activity of the metal M in CuN_4-MN_4.

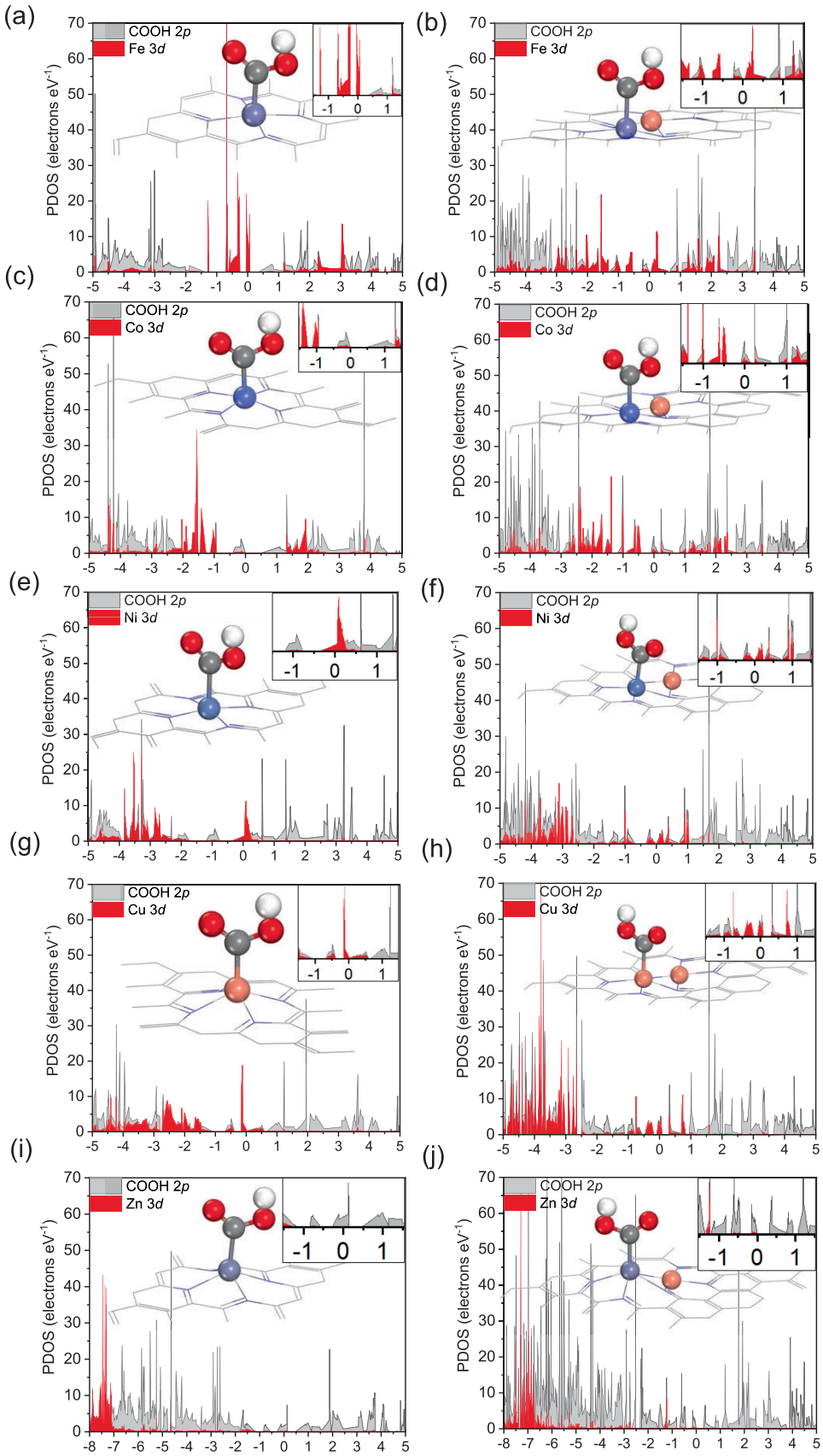

Fig. 8. Electronic PDOS of *COOH on (a) FeN_4, (b) FeN_4-CuN_4, (c) CoN_4, (d) CoN_4-CuN_4, (e) NiN_4, (f) NiN_4-CuN_4, (g) CuN_4, (h) CuN_4-CuN_4, (i) ZnN_4, and (j) ZnN_4-CuN_4. The red ball, white ball, grey ball, orange ball, and purple spheres are the O, H, C, Cu, and M (Fe, Co, Ni, and Zn) atoms, respectively.

4. Conclusions

We used DFT calculations to investigate the electrocatalytic conversion of CO_2 to C_1 chemicals (CO, HCOOH, CH_3OH, and CH_4) on two types of metal-nitrogen-doped carbon materials: SACs with structure MN_4 and DACs with structure CuN_4-MN_4 (M = Fe, Co, Ni, and Zn). The homonuclear CuN_4-CuN_4 catalyst showed improved performance only for the formation of HCOOH compared to the SAC CuN_4. However, in the heteronuclear DACs CuN_4-MN_4, the catalytic activity to form C_1 products is enhanced on the metal site M but suppressed on Cu. The Cu atom in DACs acts as a CO_2RR promoter rather than an ideal active centre.

Next, we considered the selectivity of C_1 products on SACs and DACs. We found that Cu improved CO selectivity on CuN_4-ZnN_4 but hindered it on CuN_4-FeN_4 due to strong binding between CO and the Fe site of the diatomic catalyst. For CuN_4-CoN_4, Cu regulation not only promoted CO_2RR reactivity on Co towards C_1 products, but also inhibited its competition with the hydrogen evolution reaction, resulting in higher selectivity towards carbon products than the CoN_4 SAC. Finally, we analysed the electronic properties of the catalysts and reaction intermediates to reveal the mechanism by which Cu promotes the catalytic activity of CuN_4-MN_4 DACs. Cu enhances the initial reduction of CO_2 by promoting orbital hybridization between the key intermediate *COOH 2*p*-orbitals and the neighbour metals 3*d*-orbitals around the Fermi level. This promotion effect, caused by interatomic electron transfer degree between Cu and other metals, gradually weakens from Fe to Zn due to decreasing electronegativity difference between Cu and the other metal.

This computational work, therefore, reveals a new mechanism for the role of Cu in DACs for CO_2RR, which provides instructive insights for designing practical, stable, and high-performance CO_2 electroreduction catalysts.

Declaration of competing interest

The authors declare that they have no known competing financial interests or personal relationships that could have appeared to influence the work reported in this paper.

Acknowledgments

Q.Z. thanks the China Scholarship Council for financial support. R.C.-O. acknowledges the funding by the Leverhulme Trust (RPG-2019-122). D.D.T. acknowledges the ACT program (Accelerating CCS Technologies, Horizon2020 Project No. 294766), which funded the FUNMIN project. Financial contributions were made from Department for Business, Energy & Industrial Strategy (BEIS) together with extra funding from NERC and EPSRC research councils, United Kingdom, ADEME (FR), MINECO-AEI (ES). We are grateful to the UK Materials and Molecular Modelling Hub for computational resources, which is partially funded by EPSRC (EP/P020194/1). Via our membership of the UK's HEC Materials Chemistry Consortium, which is funded by EPSRC (EP/L000202), this work used the ARCHER UK National Supercomputing Service (https://www.archer.ac.uk). This research utilized Queen Mary's Apocrita HPC facility, supported by QMUL Research-IT. https://doi.org/10.5281/zenodo.438045.

Appendix A. Supplementary material

Supplementary data to this article can be found online at https://doi.org/10.1016/j.jechem.2023.06.029.

References

[1] S.N. Talapaneni, G. Singh, I.Y. Kim, K. AlBahily, A.A.H. Al-Muhtaseb, A.S. Karakoti, E. Tavakkoli, A. Vinu, Adv. Mater. 32 (2020) 1904635.
[2] C. Lim, W.H. Lee, J.H. Won, Y.-J. Ko, S. Kim, B.K. Min, K.-Y. Lee, W.S. Jung, H.-S. Oh, Adv. Sustainable Syst. 5 (2021) 2100216.
[3] M. Sun, H.H. Wong, T. Wu, A.W. Dougherty, B. Huang, Adv. Energy Mater. 12 (2022) 2103781.
[4] Y. Quan, J. Zhu, G. Zheng, Small Sci. 1 (2021) 2100043.
[5] A. Millot, N. Maïzi, Technol. Forecast. Soc. Change 172 (2021).
[6] B.M. Tackett, E. Gomez, J.G. Chen, Nat. Catal. 2 (2019) 381–386.
[7] M. Aresta, A. Dibenedetto, A. Angelini, Chem. Rev. 114 (2014) 1709–1742.
[8] A. Mustafa, B.G. Lougou, Y. Shuai, Z. Wang, H. Tan, J. Energy Chem. 49 (2020) 96–123.
[9] Y. Zheng, A. Vasileff, X. Zhou, Y. Jiao, M. Jaroniec, S.Z. Qiao, J. Am. Chem. Soc. 141 (2019) 7646–7659.
[10] S. Nitopi, E. Bertheussen, S.B. Scott, X. Liu, A.K. Engstfeld, S. Horch, B. Seger, I.E. L. Stephens, K. Chan, C. Hahn, J.K. Nørskov, T.F. Jaramillo, I. Chorkendorff, Chem. Rev. 119 (2019) 7610–7672.
[11] S. Liu, H. Yang, X. Su, J. Ding, Q. Mao, Y. Huang, T. Zhang, B. Liu, J. Energy Chem. 36 (2019) 95–105.
[12] J. Zhu, M. Xiao, D. Ren, R. Gao, X. Liu, Z. Zhang, D. Luo, W. Xing, D. Su, A. Yu, J. Am. Chem. Soc. 144 (2022) 9661–9671.
[13] Z. Zhuang, Y. Li, J. Huang, Z. Li, K. Zhao, Y. Zhao, L. Xu, L. Zhou, L.V. Moskaleva, L. Mai, Sci. Bull. 64 (2019) 617–624.
[14] L. Zhou, R. Lv, J. Energy Chem. 70 (2022) 310–331.
[15] H. Yang, X. Wang, S. Wang, P. Zhang, C. Xiao, H.M.K. Sari, J. Liu, J. Jia, B. Cao, J. Qin, Carbon 182 (2021) 109–116.
[16] R. Daiyan, R. Chen, P. Kumar, N.M. Bedford, J. Qu, J.M. Cairney, X. Lu, R. Amal, ACS Appl. Mater. Interfaces 12 (2020) 9307–9315.
[17] H. Yang, Q. Lin, C. Zhang, X. Yu, Z. Cheng, G. Li, Q. Hu, X. Ren, Q. Zhang, J. Liu, Nat. Commun. 11 (2020) 593.
[18] S. Vijay, J.A. Gauthier, H.H. Heenen, V.J. Bukas, H.H. Kristoffersen, K. Chan, ACS Catal. 10 (2020) 7826–7835.
[19] Z. Hao, J. Chen, D. Zhang, L. Zheng, Y. Li, Z. Yin, G. He, L. Jiao, Z. Wen, X.J. Lv, Sci. Bull. 66 (2021) 1649–1658.
[20] B. Mohanty, S. Basu, B.K. Jena, J. Energy Chem. 70 (2022) 444–471.
[21] J. Li, J. Liu, B. Yang, J. Energy Chem. 53 (2021) 20–25.
[22] W. Ma, H. Wan, L. Zhang, J.Y. Zheng, Z. Zhou, J. Energy Chem. 63 (2021) 170–194.
[23] H.B. Yang, S.-F. Hung, S. Liu, K. Yuan, S. Miao, L. Zhang, X. Huang, H.-Y. Wang, W. Cai, R. Chen, Nat. Energy 3 (2018) 140–147.
[24] L. Li, Y. Huang, Y. Li, Energy Chem 2 (2020).
[25] H. Yang, Y. Wu, G. Li, Q. Lin, Q. Hu, Q. Zhang, J. Liu, C. He, J. Am. Chem. Soc. 141 (2019) 12717–12723.
[26] T. Liu, S. Ali, Z. Lian, B. Li, D.S. Su, J. Mater. Chem. A 5 (2017) 21596–21603.
[27] Z. Shi, W. Yang, Y. Gu, T. Liao, Z. Sun, Adv. Sci. 7 (2020) 2001069.
[28] Y. Yang, L. Lai, L. Wei, Y. Chen, J. Energy Chem. 63 (2021) 667–674.
[29] J. Li, P. Pršlja, T. Shinagawa, A.J. Martin Fernandez, F. Krumeich, K. Artyushkova, P. Atanassov, A. Zitolo, Y. Zhou, R. García-Muelas, ACS Catal. 9 (2019) 10426–10439.
[30] Y. Ying, X. Luo, J. Qiao, H. Huang, Adv. Funct. Mater. 31 (2021) 2007423.
[31] H. Liu, Q. Huang, W. An, Y. Wang, Y. Men, S. Liu, J. Energy Chem. 61 (2021) 507–516.
[32] Y. Wang, B.J. Park, V.K. Paidi, R. Huang, Y. Lee, K.-J. Noh, K.-S. Lee, J.W. Han, ACS Energy Lett. 7 (2022) 640–649.
[33] K. Liu, J. Li, Y. Liu, M. Wang, H. Cui, J. Energy Chem. 79 (2023) 515–534.
[34] Y. Li, W. An, J. Energy Chem. 80 (2023) 350–360.
[35] S.C. Sarma, J. Barrio, A. Bagger, A. Pedersen, M. Gong, H. Luo, M. Wang, S. Favero, C.-X. Zhao, Q. Zhang, A. Kucernak, M.-M. Titirici, I.E.L. Stephens, Adv. Funct. Mater. 9 (2023) 2302468.
[36] M. Li, H. Wang, W. Luo, P.C. Sherrell, J. Chen, J. Yang, Adv. Mater. 32 (2020) 2001848.
[37] T. Tang, Z. Wang, J. Guan, Adv. Funct. Mater. 32 (2022) 2111504.
[38] J. Hao, H. Zhu, Q. Zhao, J. Hao, S. Lu, X. Wang, F. Duan, M. Du, Nano Res. 13 (2023) 1–8.
[39] H. Cheng, X. Wu, M. Feng, X. Li, G. Lei, Z. Fan, D. Pan, F. Cui, G. He, ACS Catal. 11 (2021) 12673–12681.
[40] T. Ding, X. Liu, Z. Tao, T. Liu, T. Chen, W. Zhang, X. Shen, D. Liu, S. Wang, B. Pang, J. Am. Chem. Soc. 143 (2021) 11317–11324.
[41] H. Han, J. Im, M. Lee, D. Choo, Appl. Catal. B Environ. 320 (2023).
[42] G. Qu, K. Wei, K. Pan, J. Qin, J. Lv, J. Li, P. Ning, Nanoscale 15 (2023) 3666–3692.
[43] J.D. Yi, X. Gao, H. Zhou, W. Chen, Y. Wu, Angew. Chem. 134 (2022) e202212329.
[44] J. Wang, C. Liu, S. Li, Y. Li, Q. Zhang, Q. Peng, S.T. John, Z. Wu, Chem. Eng. J. 428 (2022).
[45] F. Chang, M. Xiao, R. Miao, Y. Liu, M. Ren, Z. Jia, D. Han, Y. Yuan, Z. Bai, L. Yang, Electrochem. Energy Rev. 5 (2022) 4.
[46] Y. Xue, Y. Guo, H. Cui, Z. Zhou, Small Methods 5 (2021) 2100736.
[47] K.P. Kuhl, T. Hatsukade, E.R. Cave, D.N. Abram, J. Kibsgaard, T.F. Jaramillo, J. Am. Chem. Soc. 136 (2014) 14107–14113.
[48] A.A. Peterson, F. Abild-Pedersen, F. Studt, J. Rossmeisl, J.K. Nørskov, Energy Environ. Sci. 3 (2010) 1311–1315.
[49] K.P. Kuhl, E.R. Cave, D.N. Abram, T.F. Jaramillo, Energy Environ. Sci. 5 (2012) 7050–7059.

[50] E. Boutin, M. Wang, J.C. Lin, M. Mesnage, D. Mendoza, B. Lassalle-Kaiser, C. Hahn, T.F. Jaramillo, M. Robert, Angew. Chem. Int. Ed. 58 (2019) 16172–16176.
[51] Y. Wu, Z. Jiang, X. Lu, Y. Liang, H. Wang, Nature 575 (2019) 639–642.
[52] F. Wang, H. Xie, T. Liu, Y. Wu, B. Chen, Appl. Energy 269 (2020).
[53] J. Hao, Z. Zhuang, J. Hao, C. Wang, S. Lu, F. Duan, F. Xu, M. Du, H. Zhu, Adv. Energy Mater. 12 (2022) 2200579.
[54] X. Wei, S. Wei, S. Cao, Y. Hu, S. Zhou, S. Liu, Z. Wang, X. Lu, Appl. Surf. Sci. 564 (2021).
[55] G. Kresse, J. Furthmüller, J. Phys.l Rev. B 54 (1996) 11169.
[56] G. Kresse, J. Furthmüller, J. Comput. Mater. Sci. 6 (1996) 15–50.
[57] M. Dion, H. Rydberg, E. Schröder, D. Langreth, B. Lundqvist, J. Phys. Rev. Lett. 95 (2005).
[58] J. Klimeš, D.R. Bowler, A. Michaelides, J. Phys. Condensed Matter. 22 (2009).
[59] H.J. Monkhorst, J.D. Pack, J. Phys. Rev. B 13 (1976) 5188.
[60] M. Yu, D.R. Trinkle, J. Chem. Phys. 134 (2011).
[61] V. Wang, N. Xu, J.-C. Liu, G. Tang, W.-T. Geng, Comput. Phys. Commun. 267 (2021).
[62] J.K. Nørskov, J. Rossmeisl, A. Logadottir, L. Lindqvist, J.R. Kitchin, T. Bligaard, H. Jonsson, J. Phys. Chem. B 108 (2004) 17886–17892.
[63] J.-H. Liu, L.-M. Yang, E. Ganz, J. Mater. Chem. A 7 (2019) (1952) 11944–111941.
[64] J. Greeley, J.K. Nørskov, Electrochim. Acta 52 (2007) 5829–5836.
[65] X. Guo, J. Gu, S. Lin, S. Zhang, Z. Chen, S. Huang, J. Am. Chem. 142 (2020) 5709–5721.
[66] T.N. Huan, N. Ranjbar, G. Rousse, M. Sougrati, A. Zitolo, V. Mougel, F. Jaouen, M. Fontecave, ACS Catal. 7 (2017) 1520–1525.
[67] C. Zhao, X. Dai, T. Yao, W. Chen, X. Wang, J. Wang, J. Yang, S. Wei, Y. Wu, Y. Li, J. Am. Chem. Soc. 139 (2017) 8078–8081.
[68] T. Wang, H. Xie, M. Chen, A. D'Aloia, J. Cho, G. Wu, Q. Li, Nano Energy 42 (2017) 69–89.
[69] L. Kong, M. Wang, L. Jiang, Chem. Asian J. 17 (2022) e202200939.
[70] J. Wang, C. Liu, S. Li, Y. Li, Q. Zhang, Q. Peng, J.S. Tse, Z. Wu, Chem. Eng. J. 428 (2022).
[71] C. Wang, C. Zhu, M. Zhang, Y. Geng, Z. Su, Adv. Theory Simul. 3 (2020) 2000218.
[72] M. Ma, Q. Tang, J. Mater. Chem. C 10 (2022) 15948–15956.
[73] A.G. Nabi, A. Hussain, G.A. Chass, D. Di Tommaso, Nanomaterials 13 (2022) 87.
[74] A. Muthuperiyanayagam, A.G. Nabi, Q. Zhao, D. Di Tommaso, Phys. Chem. Chem. Phys. 25 (2023) 13429–13441.
[75] N. Corbin, J. Zeng, K. Williams, K. Manthiram, Nano Res. 12 (2019) 2093–2125.
[76] H. Shin, K.U. Hansen, F. Jiao, Nat. Sustain. 4 (2021) 911–919.
[77] C. Guo, T. Zhang, X. Liang, X. Deng, W. Guo, Z. Wang, X. Lu, C.-M.-L. Wu, Appl. Surf. Sci. 533 (2020).
[78] S. Jiao, X. Fu, H. Huang, Adv. Funct. Mater. 32 (2022) 2107651.